Applied Water Science (2026) 16:2
https://doi.org/10.1007/s13201-025-02673-1

ORIGINAL ARTICLE

Mechanistic insights and process optimization of perilla frutescens stem biochar for cadmium removal from zinc smelter wastewater

Jae-In Lee[1] · Jun-Sik Jo[2] · Youn-Jun Lee[3] · Chang-Gu Lee[3,4] · Young-Man Yoon[5] · Seong-Jik Park[1,2]

Received: 4 July 2025 / Accepted: 16 October 2025

Abstract

Cadmium (Cd), a hazardous heavy metal primarily emitted by smelting industries, presents significant environmental and health hazards due to its persistence and strong potential for bioaccumulation. Substantial amounts of *Perilla frutescens* stems (PFS), which constitute a major agricultural byproduct, are typically discarded or openly burned in fields, thereby generating smoke, particulate emissions, and greenhouse gases. This study explored a sustainable valorization pathway by converting PFS into biochar (PFSB) via pyrolysis at temperatures ranging from 300 to 750 °C, assessing its effectiveness as an adsorbent for Cd removal. Of the evaluated biochars, the sample produced at 450 °C (PFSB–450) demonstrated desirable physicochemical characteristics, such as a high C/N ratio, low H/C ratio, well-developed porosity, and a rich presence of oxygen-containing functional groups. Batch adsorption tests showed a peak Cd adsorption capacity of 75.74 mg/g, aligning with or exceeding those of other biochar-based adsorbents reported in the literature. Notably, this level of performance was attained using a straightforward pyrolysis technique without requiring chemical modification or intricate processing steps. The adsorption processes conformed to the Elovich and Langmuir models, signifying that both chemisorption and monolayer adsorption took place. Mechanistic studies identified electrostatic attraction, ion exchange, and Cd–O/Cd–π interactions as the principal adsorption mechanisms. Response surface methodology revealed that adsorbent dosage, initial pH, and reaction time played critical roles in determining Cd removal efficacy, while temperature was found to be insignificant. Under optimized operational parameters, PFSB–450 removed 80.84% of Cd from authentic zinc smelter wastewater samples. This work illustrates the dual advantages of mitigating air pollution through agricultural residue utilization and addressing heavy metal contamination in industrial effluents, promoting a scalable and cost-efficient solution consonant with circular economy practices.

Keywords Adsorption · Agricultural byproduct · Biochar · Cadmium · Industrial wastewater

Communicated by Achlesh Daverey.

✉ Seong-Jik Park
parkseongjik@hknu.ac.kr

[1] Institute of Agricultural Environmental Science, Hankyong National University, Anseong 17579, Republic of Korea

[2] Department of Bioresources and Rural System Engineering, Hankyong National University, Anseong 17579, Republic of Korea

[3] Energy Systems Research, Ajou University, Suwon 16499, Republic of Korea

[4] Department of Environmental and Safety Engineering, Ajou University, Suwon 16499, Republic of Korea

[5] Department of Plant Life & Environmental Science, Hankyong National University, Anseong 17579, Republic of Korea

List of symbols

ANOVA	Analysis of variance
BET	Brunauer–Emmett–Teller
C	Intercept value of the intraparticle diffusion model (mg/g)
Cd_PFSB–450	PFSB–450 with Cd adsorbed
C_e	Residual Cd concentration in solution after adsorption reaction (mg/L)
D	Fractal dimension
EA	Automated elemental analyzer
EBC	European biochar certificate
FE–SEM/EDX	Field emission scanning electron microscope coupled with energy dispersive x-ray spectroscopy
FHH	Frenkel–Halsey–Hill method
FT–IR	Fourier transform infrared spectroscopy
IBI	International Biochar Initiative

Published online: 09 December 2025

ICP–OES	Inductively coupled plasma optical emission spectroscopy
IPD	Intraparticle diffusion
k_1	Pseudo-first-order kinetic rate constant (1/h)
k_2	Pseudo-second-order kinetic rate constant (mg/(g·h))
K_F	Distribution coefficient ((mg/g) (L/mg)$^{1/n}$)
k_i	Intraparticle diffusion rate constant (mg/(g·h$^{1/2}$))
K_L	Langmuir constant associated with binding energy (L/mg)
n	Freundlich constant
PFO	Pseudo-first-order
PFS	*Perilla frutescens* stems
PFSB	*Perilla frutescens* stems biochar
PFSB–300	*Perilla frutescens* stems biochar produced at 300 °C
PFSB–450	*Perilla frutescens* stems biochar produced at 450 °C
PFSB–600	*Perilla frutescens* stems biochar produced at 600 °C
PFSB–750	*Perilla frutescens* stems biochar produced at 750 °C
PSO	Pseudo-second-order
q_e	Equilibrium adsorption amount of Cd by PFSB (mg/g)
q_t	Adsorption amount of Cd by PFSB at time t (mg/g)
R^2	Coefficient of determination
RSM	Response surface methodology
t	Reaction time (h)
TGA/DTG	Thermogravimetric/derivative thermogravimetry analysis
WHO	World Health Organization
X_1	Dose of PFSB–450 (g/L)
X_2	Industrial wastewater pH
X_3	Reaction time (h)
X_4	Reaction temperature (°C)
XPS	X-ray photoelectron spectroscopy
XRF	X-ray fluorescence analysis
β	Desorption constant associated with the activation energy for chemisorption (g/mg)

Introduction

Among heavy metals, cadmium (Cd) is recognized as one of the most hazardous contaminants, occupying a leading position on the agency for toxic substances and disease registry's substance priority list (Kumar et al. 2022). The emission of Cd into the environment arises from a variety of anthropogenic sources, including zinc smelting, ceramics production, alkaline battery manufacturing, electroplating, mining activities, waste incineration, use of industrial fertilizers, and the combustion of certain types of coal and oil (Kwikima et al. 2021; Xu et al. 2022). It is estimated that approximately 7,000 ton/year of Cd are annually discharged into the environment (Segneanu et al. 2022). Prolonged exposure to Cd may result in a range of significant health problems, including but not limited to neurological disorders, respiratory illnesses, renal impairment, skeletal abnormalities, and cardiovascular conditions (Chai et al.2020; Boulanouar et al. 2025). The World Health Organization (WHO) has established a permissible limit for Cd in drinking water of 0.003 mg/L (Othmani et al. 2022).

Various methods are available for the removal of Cd from industrial wastewater, such as chemical precipitation, filtration, electrochemical treatment, ion exchange, membrane separation, and adsorption, with adsorption receiving increased research interest (Cheng et al. 2021; Xu et al. 2022; Ma et al. 2023; Lee et al. 2024a). Although membrane separation, chemical precipitation, and electrochemical treatments are effective for removing Cd, these methods are frequently hindered by significant disadvantages, including high operational costs, excessive sludge generation, and increased energy input (Gupta et al. 2021). In comparison, adsorption is considered a straightforward, cost-efficient, and environmentally benign technology, with reduced production of sludge and lower energy requirements relative to alternative methods (Liu et al. 2022a; Li et al. 2023; Shewatatek et al. 2025). The adsorption process's efficiency is heavily influenced by the type of adsorbent selected (Khan et al. 2020). Nevertheless, the high cost of some commercial adsorbents restricts their application on a large scale. Therefore, it is necessary to develop economical alternatives (Cheng et al. 2022).

Among the various biomass sources as feedstock for biochar production, agricultural residues have garnered notable attention due to their abundance, cost-effectiveness, and straightforward collection, especially within rural and agricultural regions (Yuan et al. 2021). Major components of agricultural residues include hemicellulose, cellulose, and lignin (Khedulkar et al. 2023). Traditionally, crop residues have been subject to open field burning to expedite disposal. Unfortunately, this practice significantly increases fire risks and generates serious air pollution due to the uncontrolled emission of pollutants such as CO_2, SO_2, NO_x, and particulate matter (Cho et al. 2023a). Alternatively, pyrolysis represents a controlled thermal processing technique that limits the release of hazardous gases and offers a more environmentally sound method for agricultural waste management (Awogbemi and Von Kallon 2023). The application of agricultural waste-derived biochar for Cd removal not

only contributes to the treatment of industrial wastewater but also enhances the value of agricultural residues through their conversion into beneficial products (Khedulkar et al. 2023). The adoption of this strategy advances the circular economy, lowers waste handling expenses, and delivers a sustainable means to alleviate environmental pressures (Khedulkar et al. 2023; Khelali et al. 2025).

Perilla frutescens is extensively grown and used as a food source in several Asian nations, including Korea (Niazi et al. 2018). As of 2023, Korea reported an annual production of 47,800 tons. Nevertheless, a considerable quantity of the stems is treated as agricultural waste. Owing to their lignocellulosic makeup, these residues resist rapid biodegradation. As a common disposal method, farmers burn these materials in open fields, posing substantial fire risks and contributing to atmospheric pollution related to the combustion of agricultural biomass.

In this study, discarded residues of *Perilla frutescens* stems (PFS), which otherwise present environmental risks when subjected to open-field burning, were transformed into biochar and evaluated as an adsorbent for Cd removal from wastewater. While considerable research has established that biochars derived from diverse biomass sources can achieve high Cd removal efficiencies (Othmani et al. 2022; Ma et al. 2023; Lee et al. 2024b, c), the majority of these studies have concentrated on synthetic wastewater, and research utilizing actual wastewater is scarce. To fill this research gap and improve real-world applicability, this study assessed the efficacy of PFS-derived biochar (PFSB) in removing Cd from genuine zinc smelter wastewater. PFSBs were generated at various pyrolysis temperatures, and their physicochemical characteristics were systematically analyzed to clarify the adsorption mechanism. Batch experiments were performed to identify the optimal pyrolysis temperature for Cd removal, followed by an evaluation of adsorption behavior across a range of reaction times and initial Cd concentrations. In addition, response surface methodology (RSM) was used to explore the influence of key operational parameters on Cd removal from actual zinc smelter wastewater, with the aim of optimizing treatment conditions.

Materials and methods

Adsorbent preparation

The PFS was harvested from an upland field in Hwaseong, Republic of Korea. After harvesting, the plants underwent air-drying and then threshing to separate the seeds (*Perilla frutescens*), using only the stems for this study. The obtained PFS was rinsed with tap water to eliminate soil and impurities. The cleaned PFS was then oven-dried at 65 °C for 72 h in a forced convection oven (OF–22GW, Jeio Tech Co., Ltd., Korea), ensuring complete removal of moisture. Subsequently, the dried PFS was ground using a high-speed blender (KCBL100, Foshan Leweimei Electrical Appliances Co., Ltd., China) to a particle size < 0.425 mm. Pyrolysis was performed in an oxygen-free environment utilizing a high-temperature tube furnace (STF–1250, U1tech, Korea) with N_2 gas injection capability. The heating rate during pyrolysis was set at 20 °C/min, and the target temperature was held for 1 h once reached. Pyrolysis was conducted at 300, 450, 600, and 750 °C, and the resulting biochars were designated as PFSB–300, PFSB–450, PFSB–600, and PFSB–750, respectively.

Chemicals and real zinc smelter wastewater used in this study

The Cd adsorption performance of PFSB was assessed by preparing a Cd solution with cadmium nitrate tetrahydrate ($Cd(NO_3)_2{\cdot}4H_2O$). Hydrochloric acid (HCl) and sodium hydroxide (NaOH), each at a 1 M concentration, were used to adjust the solution pH during the experiments. All reagents, purchased as extra pure grade from Samchun Chemicals, a local supplier in South Korea, were dissolved in deionized water (Direct–Q3UV, Millipore, USA) for solution preparation. The Cd solution was made and diluted in accordance with the experimental requirements.

This study investigated the practical application of PFSB for Cd removal using real wastewater collected from a zinc smelter factory. The characteristics and sampling location of the wastewater employed in this study have been comprehensively reported in our previous publications (Cho et al. 2023b; Lee et al. 2024a). Before conducting the experiment, heavy metal and inorganic cation concentrations in the zinc smelter wastewater were determined using inductively coupled plasma optical emission spectroscopy (ICP–OES, Agilent 5100, Agilent Technologies, USA). Detailed concentrations of the wastewater are summarized in Table S1. Of the heavy metals analyzed, Cd was present at the third highest level, quantified at 94.9 mg/L.

Adsorbent characterization

Characterization was performed to investigate the physicochemical changes of PFSBs resulting from the pyrolysis of PFS. The surface morphology, porosity, and physical parameters, such as specific surface area, pore volume, and pore size, were assessed using a field emission scanning electron microscope/energy dispersive X-ray spectroscopy (FE–SEM/EDX; SU8600, Hitachi, Japan) in conjunction with a specific surface area analyzer (BET; BELSORP MAX, BETMICROTRAC, Japan). The contents of C, H, N, and S in PFS and PFSBs produced at various pyrolysis temperatures were quantified by an automatic elemental

analyzer (EA; FlashSmart, Thermo Fisher, USA) to assess the elemental changes induced by pyrolysis. In addition, the elemental composition and content in PFS and PFSBs were determined using X-ray fluorescence spectrometry (XRF; S8 TIGER, Bruker AXS, USA). To evaluate the release of cations, PFS and PFSBs (3.33 g/L) were separately reacted with 30 mL of deionized water, and cation concentrations in the eluate were determined by ICP–OES. Weight variations in PFS during progressive thermal treatment were analyzed by thermogravimetric/derivative thermogravimetry analysis (TGA/DTG; TG209F1 ASC, NETZSCH, Germany). Fourier transform infrared spectroscopy (FT–IR; INVENIO–R, Bruker, USA) was applied to examine the functional groups on PFS and PFSBs.

To investigate the mechanism of Cd adsorption, characterization was carried out using FE–SEM/EDX, XRF, and X-ray photoelectron spectroscopy (XPS; K–Alpha+, Thermo Fisher Scientific, United Kingdom). The presence of Cd on PFSB following Cd adsorption was visualized by mapping Cd on FE–SEM images with EDX analysis. XRF analysis was performed to verify the presence of Cd on PFSB after adsorption. The chemical properties of PFSB before and after Cd adsorption were examined using XPS with Al Kα radiation (hv = 1253.6 eV), providing insight into the dominant adsorption mechanisms.

Adsorption experiment

Cd adsorption by PFSBs was examined as a function of both the raw material (PFS) and the pyrolysis temperature. A 3.33 g/L suspension of either PFS or PFSBs was mixed with 30 mL of a 100 mg/L Cd solution in a 50 mL conical tube and allowed to react for 24 h. Adsorption amount was determined by calculating the difference between the initial and final Cd concentrations following the reaction. The PFSB demonstrating the highest adsorption efficiency (PFSB–450) was chosen for detailed kinetic and isotherm studies. Adsorption kinetics and isotherms were evaluated using established models. For kinetic analysis, 3.33 g/L of PFSB–450 was reacted with a 400 mg/L Cd solution in a 50 mL conical tube at various time intervals (0.25, 0.5, 1, 2, 3, 6, 12, and 24 h). The experiments were conducted at an agitation speed of 100 rpm and a constant temperature of 25 °C. Both agitation speed and temperature were controlled using a temperature-regulated shaker (SJ–808SF, Sejong Scientific Co., Ltd., Korea). Isotherm adsorption experiments utilized 3.33 g/L of PFSB–450 mixed with Cd solutions varying in concentration from 100 to 1000 mg/L, in increments of 100 mg/L in a 50 mL conical tubes and were conducted for 24 h. The agitation speed and temperature conditions for isotherm studies mirrored those of the kinetic experiments (100 rpm, 25 °C). Each adsorption test was performed in triplicate under identical conditions. After kinetic and isotherm experiments, PFSB–450 was recovered from the solutions using a 0.45 µm cellulose acetate filter paper (Advantec, Japan). Residual Cd concentrations after material separation were measured by ICP–OES at a wavelength of 226.502 nm. The PFSB–450 retrieved post-Cd adsorption was subsequently characterized to investigate the underlying Cd adsorption mechanism.

For kinetic and isotherm model analyses, the mean values from three independent experiments were employed. Associated error bars are reported in the relevant figures. Pseudo-first-order (PFO), pseudo-second-order (PSO), Elovich, and intraparticle diffusion (IPD) models were applied to interpret the adsorption kinetics. Langmuir and Freundlich models were utilized for isotherm assessments. The mathematical expressions for all kinetic and isotherm models are provided in the Supplementary Information. All procedures were conducted in triplicate. Data were subjected to analysis of variance (ANOVA) and further evaluated by Duncan's multiple range test to establish statistical differences. Statistical analysis was performed using IBM SPSS Statistics software (SPSS Inc., Chicago, IL, USA), with statistical significance declared at p-value < 0.05.

The reusability of PFSB–450 for Cd adsorption was assessed through three sequential adsorption–desorption cycles. Initially, 3.33 g/L of PFSB–450 was mixed with 400 mg/L cadmium solution and allowed to react for 24 h. Following the reaction, the used PFSB–450 was isolated from the solution and subsequently dried. The dried PFSB–450 was then subjected to washing by mixing with deionized water for 24 h. This adsorption–desorption sequence was repeated for three cycles to evaluate the material's regeneration capacity.

Response surface methodology for Cd adsorption on PFSB

The efficiency of PFSB in removing Cd from actual industrial wastewater was studied using response surface methodology (RSM). A Box–Behnken design, a widely adopted method within RSM, was applied to investigate the interactions among multiple independent variables and to develop a statistical model. The chosen independent variables were PFSB–450 dose (X_1, g/L), industrial wastewater pH (X_2), reaction duration (X_3, h), and reaction temperature (X_4, °C). The specific values for these variables are listed in Table S2. A total of 29 experimental conditions were generated using statistical software (version 7.0.0, Stat-Ease Inc., Minneapolis, MN, USA) by systematically varying the four factors. Adsorption trials were then conducted following the software-generated conditions, according to the batch adsorption experiment outlined in Sect. "Adsorption experiment". Prior to experimentation, the pH of the industrial wastewater was adjusted as needed with 1 M HCl or NaOH. The collected

experimental data were used to construct a polynomial regression model, and its statistical relevance was analyzed using ANOVA.

Results and discussion

Characterization of PFS and PFSB according to pyrolysis temperature

The main parameters that influence biochar production include biomass feedstock type, pyrolysis temperature, heating rate, inert gas flow rate, and residence time (Sekhon et al. 2021). Of these, pyrolysis temperature is especially critical for modifying the physicochemical properties of the feedstock, thus impacting both the quality and applicability of the resulting biochar (Panwar and Pawar 2022). In this research, the effects of pyrolysis temperature on the physicochemical properties of PFSBs were systematically analyzed.

FE–SEM was employed to investigate the surface morphologies of PFS and PFSB synthesized at varying pyrolysis temperatures. Representative FE–SEM micrographs are shown in Fig. 1(a). The surface of PFS exhibited a smoother and more planar appearance compared to that of PFSB. With increasing pyrolysis temperature, the surface of PFSB developed noticeable cracks, resulting in increased surface roughness and the emergence of pore structures. The formation of these cracks likely arose from the decomposition and evolution of carbon dioxide, methane, water, and volatile constituents during the pyrolysis process (Jeon et al. 2019; Oginni et al. 2020). The heterogeneous and rough surface topology observed in PFSB could be beneficial for improving adsorption capacity (Ahmed et al. 2020).

Table 1 presents the results for specific surface areas, pore volumes, and pore sizes of PFS and PFSB. Although the specific surface area typically increased as pyrolysis temperature rose, substantial changes in PFSBs were observed only for PFSB–750. Pore sizes of both PFS and PFSBs (except for PFSB–750) fell within the range of 2 nm to 50 nm, confirming that these materials consisted of mesopores (Gan et al. 2021). In contrast, the pore size of PFSB–750 was determined as 1.8 nm, indicating its principal composition of micropores (< 2 nm) rather than mesopores (Gan et al. 2021). The Frenkel–Halsey–Hill (FHH) model was used to calculate the fractal dimension *(D)*, thereby quantifying the surface roughness and structural irregularity of the pores (Li et al. 2019). The determined D value ranged from $2 \leq D < 3$, with higher D values corresponding to rougher pore surfaces and more heterogeneous pore size distributions (Wang et al. 2022a). Both PFS and PFSBs demonstrated rough pore surfaces and heterogeneity in pore size distribution. The pore size distributions of PFS and PFSBs were assessed via nonlocal density functional theory (NLDFT), drawing on BET data. Figure 1(b) displays the pore size distributions for each sample. PFS possessed a comparatively wide pore size distribution from 1–90 nm. Following pyrolysis, the pore sizes became increasingly concentrated below 40 nm. Although PFSB–450 and PFSB–600 did not display significant alterations in pore size distribution compared to PFSB–300, both exhibited an increased total pore volume. For PFSB–750, the pore size sharply diminished and was concentrated under 2 nm, coinciding with an almost tenfold increase in pore volume.

The contents of C, N, H, and S in both PFS and PFSB were determined, and the H/C ratio was calculated. The findings are shown in Table 1. In comparison with PFS, PFSB demonstrated an increase in C content and a reduction in H content as the pyrolysis temperature rose. This behavior is ascribed to the intensification of the carbonization process, which results from dehydrogenation reactions occurring during pyrolysis (Fan et al. 2022). All PFSB samples obtained at various pyrolysis temperatures had H/C ratios below 0.7, fulfilling the classification criteria for biochar set by the international biochar initiative (IBI) and the European biochar certificate (EBC) (Balmuk et al. 2023). The H/C ratio serves as an indicator of the extent of thermochemical transformation that biomass undergoes during pyrolysis, where a lower H/C value reflects greater aromaticity (Xu et al. 2021; Wang et al. 2022b). Furthermore, a higher C/N ratio is also indicative of increased aromaticity in biochar (Das et al. 2021). The H/C ratio for PFSB decreased as pyrolysis temperature increased. These findings demonstrate that higher pyrolysis temperatures enhance carbonization, result in the loss of polar functional groups, and promote the development of a more stable aromatic structure in PFSB (Das et al. 2021).

The major elemental compositions of PFS and PFSBs, determined by XRF analysis, are shown in Table 1. The primary elements detected in both PFS and PFSBs included C, K, Ca, and P, with C as the predominant component. With increasing pyrolysis temperature, the contents of K, Ca, and P displayed a clear upward trend. The concentrations of cations leached from PFS and PFSBs are quantified in Table 1. Among the leached cations, K^+ was the most prevalent in all analyzed samples. An elevation in cation concentrations was observed as the pyrolysis temperature of PFSB increased. Cations such as K^+, Ca^{2+}, Mg^{2+}, and Al^{3+} remain in the biochar matrix either through direct electrostatic attraction or as complexes formed with carboxyl and hydroxyl groups (Lu et al. 2023). These cations contribute to ion-exchange adsorption mechanisms, which enhance the capability for Cd adsorption (Wu et al. 2019; Gao et al. 2023).

Weight loss of PFS during pyrolysis was assessed via TGA/DTG, and the findings are displayed in Fig. 1(c). During pyrolysis, PFS underwent distinct weight loss phases at characteristic temperatures, attributed to progressive

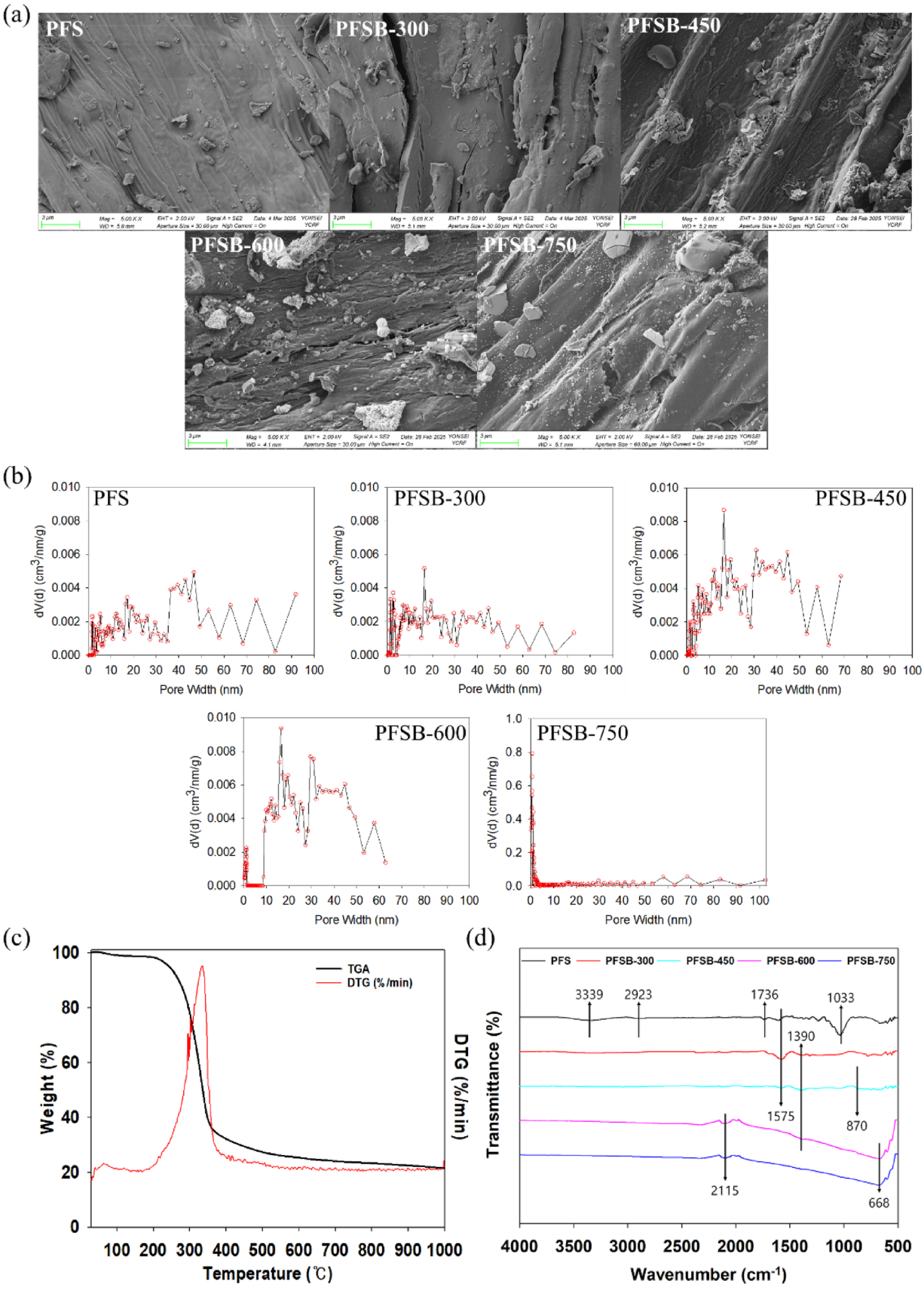
(a)
PFS
PFSB-300
PFSB-450
PFSB-600
PFSB-750
(b)
PFS
PFSB-300
PFSB-450
PFSB-600
PFSB-750
dV(d) (cm3/nm/g)
Pore Width (nm)
(c)
TGA
DTG (%/min)
Weight (%)
DTG (%/min)
Temperature (℃)
(d)
PFS
PFSB-300
PFSB-450
PFSB-600
PFSB-750
3339
2923
1736
1033
1390
1575
870
2115
668
Transmittance (%)
Wavenumber (cm-1)

◂**Fig. 1** (a) FE–SEM images depicting surface morphology, (b) Pore size distributions of PFS and PFSB generated at various pyrolysis temperatures, (c) TGA/DTG profiles specifically for PFS, and (d) FT–IR spectra of PFS and PFSB produced under different pyrolysis temperature conditions

decomposition of its constituents. Weight loss detected in the 50–180 °C range resulted from the evaporation of water retained in PFS (Rasapoor et al. 2020). The majority of PFS weight loss, exceeding 60% of the total, occurred between 200–400 °C. This temperature interval corresponds to the decomposition of hemicellulose and cellulose (de Paula Protásio et al. 2022). The most pronounced decomposition of hemicellulose and cellulose occurs from 200 to 350 °C, although cellulose continues to degrade, to a lesser extent, up to 500 °C (Pasumarthi et al. 2024). Moreover, a minor yet continuous weight loss observed above 400 °C was associated with lignin decomposition (Mishra et al. 2025).

Functional groups of PFS and PFSBs were characterized using FT–IR spectroscopy. Representative peaks are displayed in Fig. 1(d). The feedstock PFS showed distinct FT–IR peaks assigned to specific functional groups, which differed from those of PFSB. The peak at 3339 cm^{-1} is associated with O–H stretching, attributed to water present in PFS (Tomczyk et al. 2020). The signal at 2923 cm^{-1} was linked to alkyl –CH– stretching vibrations, indicative of cellulose and hemicellulose presence (Chen et al. 2020). A peak at 1736 cm^{-1}, assigned to –C = O stretching, reflected the presence of hemicellulose (Vikraman et al. 2021). The band observed at 1033 cm^{-1} within the 1100–1000 cm^{-1} region corresponded to C–O stretching vibrations of hemicellulose (Waqas et al. 2018). In contrast, these peaks were absent in PFSB, which was attributed to water loss and the thermal degradation of hemicellulose and cellulose during pyrolysis. This process facilitates the evolution of hydrogen and oxygen as CO_2 and CH_4 (Khiari et al. 2020). This observation is consistent with TGA results, demonstrating the breakdown of hemicellulose and cellulose beginning at 200 °C. The peak at 1575 cm^{-1} detected in PFS, PFSB–300, and PFSB–450 corresponds to the aromatic skeletal stretching (C = C) of lignin (Rechberger et al. 2019; Li et al. 2020). The disappearance of this peak in PFSB–600 and PFSB–750 indicates that lignin undergoes decomposition at pyrolysis temperatures above 600 °C. The 1390 cm^{-1} peak observed in PFSB–300, PFSB–450, and PFSB–600 is attributed to the C = C bond of carboxyl groups (Abdel-Rhman et al. 2023; Chang et al. 2024). The intensity of this band progressively decreased with increasing pyrolysis temperatures from 300 to 600 °C. Distinct peaks detected exclusively in PFSB–600 and PFSB–750 at 2115 cm^{-1} and 668 cm^{-1} were assigned to C≡C and C = C groups, respectively, suggesting the development of aromatic carbon structures (Kolesnikov et al. 2022; Thangaraj et al. 2024). The unique peak at 870 cm^{-1} observed only in PFSB–450 is ascribed to C–O–O stretching, reflecting the existence of oxygen-containing functional groups (Atta et al. 2022). The influence of these oxygen-containing functional groups on Cd adsorption is examined in Sect. "Cd adsorption mechanism".

The Cd adsorption performance of PFS and PFSB synthesized at various pyrolysis temperatures was investigated. The results are shown in Fig. 2. A notable enhancement in Cd adsorption capacity was recorded as the pyrolysis temperature increased from 300 to 450 °C. However, when the pyrolysis temperature surpassed 450 °C, both the adsorption capacity and removal efficiency exhibited minimal further improvement. Consequently, PFSB–450, produced at a comparatively lower temperature, is more advantageous for Cd removal than PFSB–600 and PFSB–750, as it offers similar removal efficiency with reduced energy consumption.

Although PFSB–750 exhibited the highest specific surface area among all evaluated samples, it did not lead to a substantial improvement in Cd removal. While a high surface area typically provides increased active sites for adsorption (Liu et al. 2022b), these results indicate that surface area is not the primary determinant of Cd adsorption capacity in biochar. Other factors, including the nature of surface functional groups, electrostatic forces, and ion exchange capacity, likely exert greater influence (Yuan et al. 2020). Earlier research also documented improved Cd adsorption even with reduced surface area, which was attributed to increased surface complexation and stronger electrostatic interactions (Liu et al. 2023). Sect. "Cd adsorption mechanism" (Cd adsorption mechanism) provides a more detailed discussion of factors affecting Cd adsorption.

Kinetic and isotherm experiments on Cd adsorption by PFSB–450

PFSB–450, identified as the most effective adsorbent for Cd removal, was chosen for further batch adsorption experiments. The outcomes of the kinetic adsorption studies performed with PFSB–450 are illustrated in Fig. 3(a). A marked increase in Cd adsorption occurred during the first 3 h of contact, after which the adsorption rate progressively declined as equilibrium was approached. In order to characterize the kinetic Cd adsorption behavior of PFSB–450, the PFO, PSO, Elovich, and IPD models were utilized. Model fitting results are provided in Fig. 3(a,b), with their corresponding calculated parameters presented in Table S3. The PFO model is based on the assumption that physical diffusion, dependent on the pollutant concentration, is the primary rate-limiting step (Vareda 2023), while the PSO and Elovich models suggest that chemisorption dictates the main rate-limiting step in the adsorption process (Chen et al. 2022; Gao et al. 2023). The Cd adsorption capacity predicted by the PSO model (68.85 mg/g) was the closest

Table 1 Specific surface areas, pore properties, fractal dimensions, C, N, H, and S compositions, mole ratio values, elemental compositions (analyzed by XRF), and concentrations of leached cations (elution) of PFS and PFSB at different pyrolysis temperatures

	Specific surface area (m^2/g)	Pore volume (cm^3/g)	Pore size (nm)	Fractal dimension (D)	EA results (wt. %)				Mole ratio		Elemental composition (wt.%)				Elution (mg/L)				
					C	H	N	S	H/C	C/N	C	K	Ca	P	K^+	Ca^{2+}	Na^+	Mg^{2+}	Al^{3+}
PFS	1.2	0.003	10.4	2.7	44.5	5.9	0.4	0.0	1.6	120.6	87.7	6.4	3.9	1.0	21.6	4.5	3.0	1.5	-
PFSB–300	2.0	0.003	6.8	2.7	63.5	3.5	0.7	0.0	0.7	102.9	70.6	16.5	9.2	1.9	43.9	3.5	2.9	1.4	-
PFSB–450	2.0	0.005	10.9	2.6	69.6	2.5	0.6	0.0	0.4	135.4	69.7	17.4	9.3	1.9	60.9	5.5	2.9	1.6	0.07
PFSB–600	2.7	0.005	7.5	2.4	71.9	1.0	0.6	0.0	0.2	133.2	65.9	19.6	10.6	2.2	73.9	8.6	3.1	2.1	0.06
PFSB–750	563.3	0.249	1.8	3.0	72.1	0.5	0.7	0.0	0.1	123.6	64.0	17.9	13.2	2.7	70.4	6.0	6.6	3.5	0.08

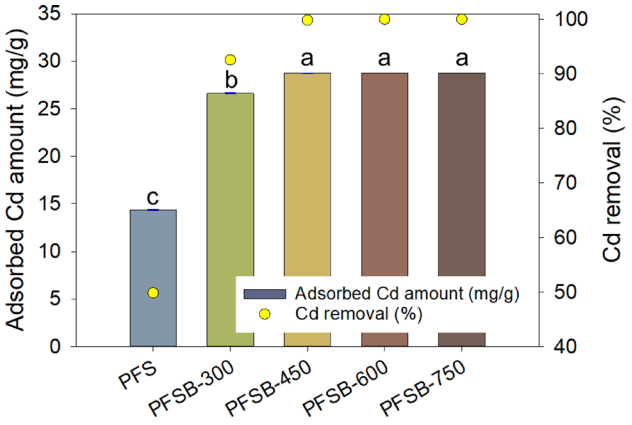

Fig. 2 Cd adsorption of PFS and PFSB at different pyrolysis temperatures

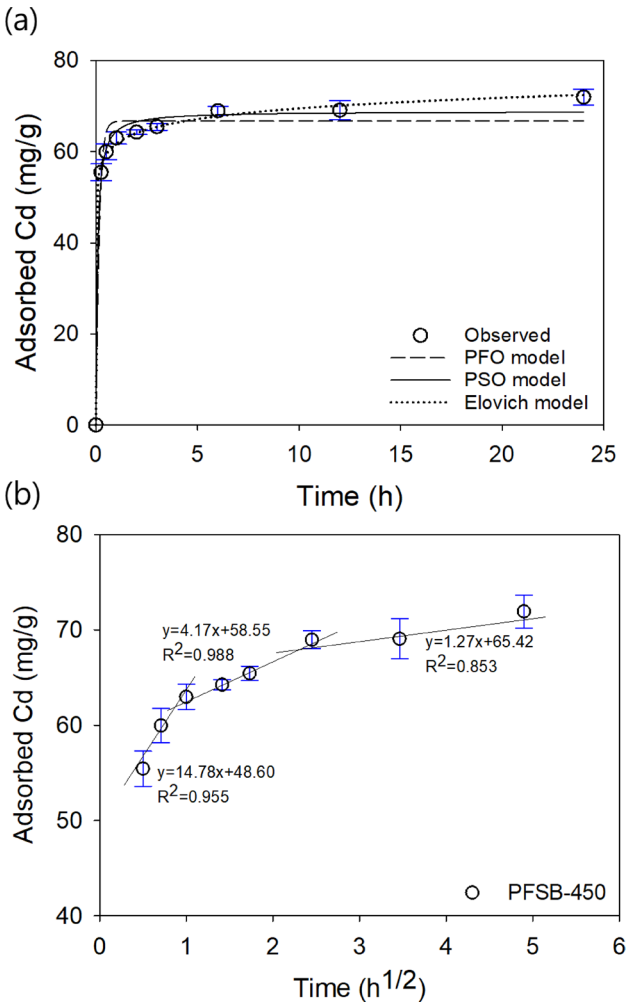

Fig. 3 (a) Impact of reaction time on Cd adsorption by PFSB–450 (PFO: pseudo-first-order, PSO: pseudo-second-order), (b) Application of the intraparticle diffusion model for Cd adsorption by PFSB–450

to the experimentally observed value (71.95 mg/g). Evaluating the coefficient of determination (R^2) revealed that the best-fitting order for Cd adsorption by PFSB–450 was Elovich > PSO > PFO. These data further support that the adsorption rate of Cd was predominantly influenced by chemisorption.

Adopting the method proposed by Wang and Guo (2020), the kinetic constants k_1 (PFO, 1/h) and k_2 (PSO, g/mg·h) were standardized to enable consistent comparison of adsorption rates across different reaction periods. A substantial increase in adsorption rate was recorded as the contact time grew from 0.25 h (k_1: 73.60 g/mg·h; k_2: 38.09 g/mg·h) to 0.5 h (k_1: 75.72 g/mg·h; k_2: 1056.49 g/mg·h), with the PSO rate displaying a particularly pronounced escalation. Subsequently, both rates steadily decreased to zero after 3 h, signifying that adsorption equilibrium had been reached. These results are consistent with experimental evidence indicating that equilibrium was achieved within 3 h.

The IPD model was categorized into three stages (0.25–1 h, 1–6 h, and 6–24 h), as depicted in Fig. 3(b). For all tested conditions, R^2 values were above 0.85, demonstrating that Cd adsorption by PFSB–450 was effectively described by the model. Since the fitted lines did not intersect the origin, intraparticle diffusion could not be considered the sole rate-limiting step (Wu et al. 2022). The slope (k_i) declined with longer reaction times, and the relatively low k_i value during 6–24 h indicates that adsorption became slower in the final stage.

Isotherm adsorption data as a function of initial Cd concentration as well as the fitting results for the Langmuir and Freundlich models are shown in Fig. S1. Parameters derived from model fitting are provided in Table S4. At an initial Cd concentration of 300 mg/L, the Cd adsorption capacity of PFSB–450 reached equilibrium, with an experimental maximum adsorption capacity of 75.74 mg/g. The maximum Cd adsorption capacity predicted by the Langmuir model (72.97 mg/g) fell within the experimental equilibrium range (69.81–75.74 mg/g). Furthermore, the Langmuir model exhibited a higher R^2 value compared to the Freundlich model, indicating its superior fit for the Cd adsorption characteristics of PFSB–450. The Langmuir model posits that adsorption takes place as a monolayer on a surface with uniform adsorption energy (Liu et al. 2022c). Additionally, in the Freundlich model, $1/n$ reflects surface heterogeneity, where $0 < 1/n < 1$ signifies a favorable adsorption process (Debnath and Das 2023). As such, Cd adsorption onto available PFSB–450 adsorption sites likely occurs predominantly in a monolayer and under favorable conditions.

The Cd adsorption capacity of PFSB–450 was evaluated and compared with other biochar-based adsorbents documented in previous research. The outcomes are presented in Table 2. Among the 13 biochars assessed, PFSB–450

Table 2 Comparison of maximum Cd adsorption capacities using various biochars reported in previous studies

Adsorbent	Q_m (mg/g)	Pyrolysis temperature (°C)	Modified	pH	Dose (g/L)	Synthetic/Actual wastewater (Removal %)	Reference
Hen manure biochar	302.00	700	-	-	1.67	Synthetic	(Lee et al. 2024b)
Thermally activated Fenton sludge	260.20	900	-	5	1.00	Actual (98.4%)	(Cho et al. 2023b)
S. europaea-derived biochar	108.54	-	-	6	0.67	Synthetic	(Ge et al. 2024)
Biochar modified with nano-MnOx	108.20	500	Nano-MnO_x	6	3.30	Synthetic	(Zhou et al. 2024)
Biochar modified with silicate (5:1)	79.66	500	$Na_2SiO_3{\cdot}9H_2O$	1	6.00	Synthetic	(Zhou et al. 2024)
Biochar modified with $MgCl_2$	78.50	600	$MgCl_2$	5	2.00	Synthetic	(Zhang et al. 2021)
PFSB–450	72.97	450	-	6	3.33	Actual sample (80.84%)	This research
Poultry manure-derived biochar	60.39	600	-	-	3.33	Actual sample (42.93%)	(Lee et al. 2024c)
Magnetic biochar derived from cow manure	58.80	800	$FeCl_3$ and $FeCl_2$-modified	-	5.00	Synthetic solution	(Li et al. 2024)
Biochar produced from straw	41.26	500	-	6	3.30	Synthetic solution	(Zhou et al. 2024)
Biochar from corn straw	38.08	500	Na_2SiO_3-modified	6	2.50	Synthetic	(Kang et al. 2024)
Z. mays biochar	14.69	-	-	6	0.67	Synthetic	(Ge et al. 2024)
Unmodified biochar	3.72	500	-	1	6.00	Synthetic	(Zhou et al. 2025)

was ranked seventh in terms of Cd adsorption capacity. If chemically modified biochars are excluded, PFSB–450 ranks fourth. Remarkably, PFSB–450 demonstrated comparable or enhanced Cd adsorption capacity relative to some chemically treated biochars, despite not utilizing chemical additives. This underscores its simpler production method and reduced environmental impact. Additionally, as PFSB–450 is solely produced from agricultural residue via pyrolysis, it presents a cost-effective, efficient, and sustainable approach attributable to its straightforward thermal conversion process. The exclusive use of agricultural waste as feedstock also lessens societal concerns and potential health risks associated with biochars made from livestock manure or industrial waste, thereby increasing its suitability for wider environmental applications.

Reusability and cost-effectiveness of PFSB–450 as a Cd adsorbent

The reusability of PFSB–450 was tested over three consecutive adsorption–desorption cycles, and the respective Cd adsorption and desorption values are illustrated in Fig. S2. Compared to the initial cycle, Cd adsorption dropped by 90.1% in the second cycle and by 98.6% in the third, revealing a significant reduction in adsorption efficiency with repeated use. Given this considerable decline in capacity after regeneration, the reuse of PFSB–450 is not advisable. Despite its low potential for regeneration, PFSB–450 remains suitable for direct application as an adsorbent, as it can be abundantly produced from agricultural by-products through low-temperature pyrolysis. These properties support its practicality for water treatment applications, eliminating the need for complicated regeneration procedures.

Given the restricted reusability of PFSB–450, its primary practical advantage is in single-use applications. Only about 10% of the initial adsorption capacity was retained following regeneration, and additional expenses would arise from wastewater generated through the regeneration process. Since

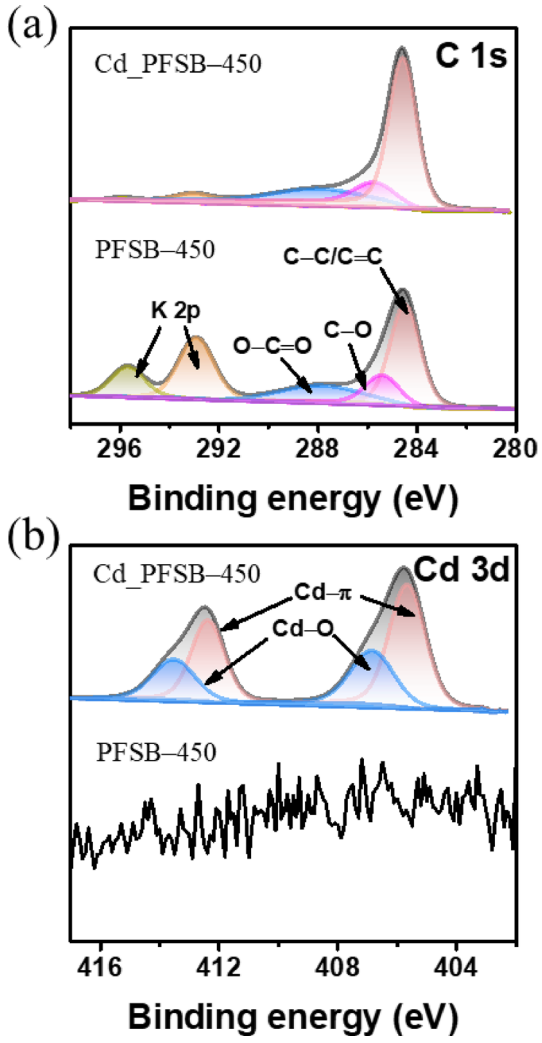

Fig. 5 (a) C 1 s and (b) Cd 3d XPS spectra of PFSB–450 and PFSB–450 following Cd adsorption

PFSB–450 is produced solely through pyrolysis without chemical additives and requires only thermal energy, it qualifies as

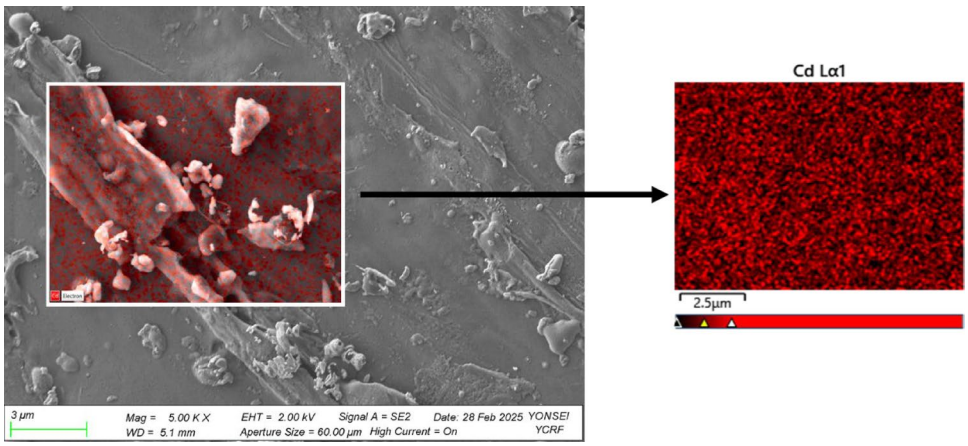

Fig. 4 Mapping image depicting the distribution of Cd on the surface of Cd-adsorbed PFSB–450 (Cd_PFSB–450)

a cost-effective adsorbent. The estimated production cost of PFSB–450 is based on electricity consumption (6.4 kWh = 733 KRW) per pyrolysis batch, processing 100 g of PFS as feedstock. Pyrolyzing 100 g of PFS at 450 °C for 1 h yielded 45 g of PFSB–450. Therefore, the total production cost for 1 kg of PFSB–450 was calculated to be approximately 16,289 KRW (equivalent to 11.8 USD), with potential for cost reduction through scaling up and optimizing the process.

Cd adsorption mechanism

Surface morphology alterations of Cd-adsorbed PFSB–450 (Cd_PFSB–450) were investigated, and the distribution of Cd was characterized using EDS and mapping techniques (Fig. 4). The initially rough surface of PFSB–450 became noticeably smoother following Cd interaction. EDS mapping indicated that Cd was homogeneously distributed over the PFSB–450 surface.

Cd was exclusively observed in Cd_PFSB–450, with a quantified Cd content of 9.5% (Table S5). This result verifies Cd adsorption onto PFSB–450. Furthermore, comparison of leached cation concentrations between PFSB–450 and Cd_PFSB–450 revealed decreases in all cations post Cd adsorption except for Na^+ (Table S5). The observed variation in cation concentrations before and after Cd adsorption indicates that K^+ and Ca^{2+} were exchanged with Cd^{2+} via electrostatic interactions. Ion exchange mechanisms involving K^+ and Ca^{2+} being substituted by Cd^{2+} are represented in Eqs. (1) and (2) (Cho et al. 2023b; Lee et al. 2024c):

$$\mathrm{PFSB{-}450} \equiv 2K^+ + Cd^{2+} \rightarrow \equiv Cd^{2+} + 2K^+ \quad (1)$$

$$\mathrm{PFSB{-}450} \equiv Ca^{2+} + Cd^{2+} \rightarrow \equiv Cd^{2+} + Ca^{2+} \quad (2)$$

The C 1 s XPS spectrum was deconvoluted into three distinct peaks attributed to C = C (284.6 eV), C–O (285.45 eV), and O–C = O (288.0 eV) (Liu et al. 2022a), with no significant spectral changes after Cd adsorption (Fig. 5). In contrast, a reduction in the intensity of peaks associated with K 2p was observed for Cd_PFSB–450 (Lee et al. 2024d). Additionally, the measured K content dramatically decreased from 8.76 to 0.56%, supporting the conclusion that ion exchange and electrostatic attraction were primary mechanisms facilitating Cd^{2+} uptake. In the Cd 3d XPS spectra (Fig. 5), newly emergent peaks corresponding to Cd–O (406.8 and 413.5 eV) and Cd–π (405.6 and 412.4 eV) interactions appeared in Cd_PFSB–450 (Cheng et al. 2021), indicating that the aromatic structure of PFSB–450 contributed to the adsorption of Cd^{2+}. The chemical equations for Cd adsorption via Cd–O (Tan et al. 2022) and Cd–π (Teng et al. 2020) are outlined below:

$$C{-}O{-}H + Cd^{2+} \rightarrow C{-}O{-}Cd^+ + H^+ \quad (3)$$

$$2C{-}COOH + Cd^{2+} \rightarrow (C{-}COO)2Cd + 2H^+ \quad (4)$$

$$C{-}\pi + Cd^{2+} \rightarrow C{-}\pi \cdots Cd^{2+} \quad (5)$$

The Cd adsorption mechanism of PFSB–450 involves multiple processes, including electrostatic attraction, ion exchange, and chemical complexation. The observed reductions in K^+ and Ca^{2+} concentrations in PFSB–450, along with the formation of Cd–O and Cd–π bonds, provide evidence that Cd^{2+} can substitute for native cations via ion exchange and associate with oxygen-containing and aromatic functional groups. The presence of oxygen-containing and aromatic functional groups in PFSB–450 was verified by its FT–IR spectrum, which exhibited characteristic peaks corresponding to aromatic skeletal stretching originating from lignin and C–O–O bonds indicative of oxygen-containing functional groups. In general, an increased surface area contributes to enhanced adsorption by providing a greater number of available adsorption sites (Leng et al. 2021). Nonetheless, despite PFSB–750 having the highest specific surface area, it did not demonstrate a higher Cd adsorption capacity compared to PFSB–450. This indicates that Cd adsorption by PFSB–450 is influenced predominantly by electrostatic interactions, ion exchange via cation replacement, and binding to oxygen-containing and aromatic functional groups rather than by surface area alone.

Response surface methodology for Cd adsorption by PFSB–450

The optimal conditions for applying PFSB–450 to actual zinc smelter wastewater were established using RSM analysis with the Box–Behnken design model. The polynomial model generated from the RSM analysis was formulated in terms of the Cd removal percentage (%):

$$\begin{aligned}\mathbf{Y}(\%) &= 36.23 + 17.54X_1 + 10.79X_2 \\ &+ 3.06X_3 + 0.18X_4 + 7.04X_1X_2 \\ &+ 2.33X_1X_3 + 0.18X_1X_4 \\ &+ 1.23X_2X_3 - 0.50X_2X_4 - 0.27X_3X_4 \\ &+ 2.96X_1^2 + 1.00X_2^2 - 1.23X_3^2 - 0.63X_4^2 \quad (6)\end{aligned}$$

The developed polynomial model was evaluated using ANOVA. These results are detailed in Table 3. In ANOVA, a high *F*-value and a *p*-value less than 0.05 confirm that the model is statistically significant and dependable (Nguyen et al. 2024). For the developed model, an *F*-value of 33.78 and a *p*-value less than 0.0001 were obtained, demonstrating its statistical relevance in predicting Cd removal with the chosen variables. The experimental data yielded an R^2 of

Table 3 Results of the analysis of variance (ANOVA) for the quadratic model of Cd removal by PFSB–450

Source	Sum of Squares	df	Mean Square	*F*-value	*p*-value (Prob > *F*)
Model	5518.13	14	394.15	33.78	< 0.0001
X_1	3692.70	1	3692.70	316.51	< 0.0001
X_2	1396.38	1	1396.38	119.69	< 0.0001
X_3	112.04	1	112.04	9.60	0.0078
X_4	0.40	1	0.40	0.03	0.8556
X_1X_2	198.37	1	198.37	17.00	0.0010
X_1X_3	21.81	1	21.81	1.87	0.1931
X_1X_4	0.12	1	0.12	0.01	0.9196
X_2X_3	6.07	1	6.07	0.52	0.4827
X_2X_4	1.01	1	1.01	0.09	0.7734
X_3X_4	0.28	1	0.28	0.02	0.8783
X_1^2	56.85	1	56.85	4.87	0.0445
X_2^2	6.47	1	6.47	0.55	0.4689
X_3^2	9.74	1	9.74	0.83	0.3765
X_4^2	2.55	1	2.55	0.22	0.6476
Residual	163.34	14	11.67		
Lack of Fit	139.37	10	13.94	2.33	0.2159
Pure Error	23.97	4	5.99		
Corrected Total	5681.46	28			

0.971 and a predicted R^2 of 0.943, both values being close to 1, thus signifying a strong correspondence between the experimental and predicted data (Polat and Sayan 2019). The R^2 value from ANOVA (0.971) indicated that 97.1% of the overall variance was accounted for by the model, with only 2.9% unexplained (Sahu et al. 2018). As the gap between the predicted R^2 (0.943) and the adjusted R^2 (0.852) was 0.09—well within the acceptable limit of less than 0.2—the model was determined to be reliable for predicting Cd removal (Igwilo et al. 2022). The signal-to-noise ratio for Cd removal using PFSB–450 was 23.06, which confirms that the model can effectively discriminate within the design space since values above 4 reflect good model discrimination ability (Alrefaee et al. 2023). Furthermore, a lack of fit *p*-value greater than 0.05 demonstrated that the polynomial model provided an adequate fit to the experimental data for Cd removal (Narzari et al. 2024).

The independent variables examined in the experiments were the dose of PFSB–450 (X_1, g/L), pH of the industrial wastewater (X_2), reaction time (X_3, h), and reaction temperature (X_4, °C). These variable values are provided in Table S2. The statistical significance of each independent variable based on ANOVA is presented in Table 3. The response surface curve and contour plots were generated by assigning a coded value of 0 (central point) for two independent variables, while varying the values of the other two variables within the developed model (Fig. 6). As shown by ANOVA, the *p*-values for X_1 (dose of PFSB–450), X_2 (pH of the industrial wastewater), and X_3 (reaction time) were less than 0.05, indicating that these variables had statistically significant effects. Moreover, the interactions X_1X_2 and X_1^2 also exhibited *p*-values below 0.05, signifying a significant relationship. In contrast, the *p*-value for X_4 (reaction temperature) was greater than 0.05, indicating its effect on Cd removal was not statistically significant.

The contour plot in Fig. 6(a) demonstrates that increasing both the dose (X_1) and pH (X_2) led to higher Cd removal percentage, exceeding 70%. In Fig. 6(b), a higher dose (X_1) combined with increased reaction time (X_3) resulted in over 60% Cd removal efficiency, especially at a dose near 39 g/L and a reaction time of 7 h. In Fig. 6(c), the Cd removal percentage showed no substantial change as X_4 varied; however, Cd removal increased with higher dose (X_1). Analysis of the contour plots identified optimal conditions for maximizing Cd removal as a PFSB–450 dose of 39.97 g/L, pH 6, reaction time of 7.94 h, and reaction temperature of 23.16 °C, which yielded a maximum Cd removal efficiency of 80.84%.

The signs of the coefficients in the developed model indicated whether each variable was positively or negatively correlated with the response (Mohammad et al. 2019). Notably, the independent variable X_1 (dose of PFSB–450) showed a positive coefficient, indicating a direct correlation with the percentage of Cd removal. This trend is attributed to the increased availability of active adsorption sites with higher doses, which enhances Cd removal efficiency (Gu et al. 2021).

The independent variable X_2 (pH of industrial wastewater) demonstrated a positive association with Cd removal efficiency, as indicated by the positive coefficient observed in the constructed model. pH plays a crucial role in

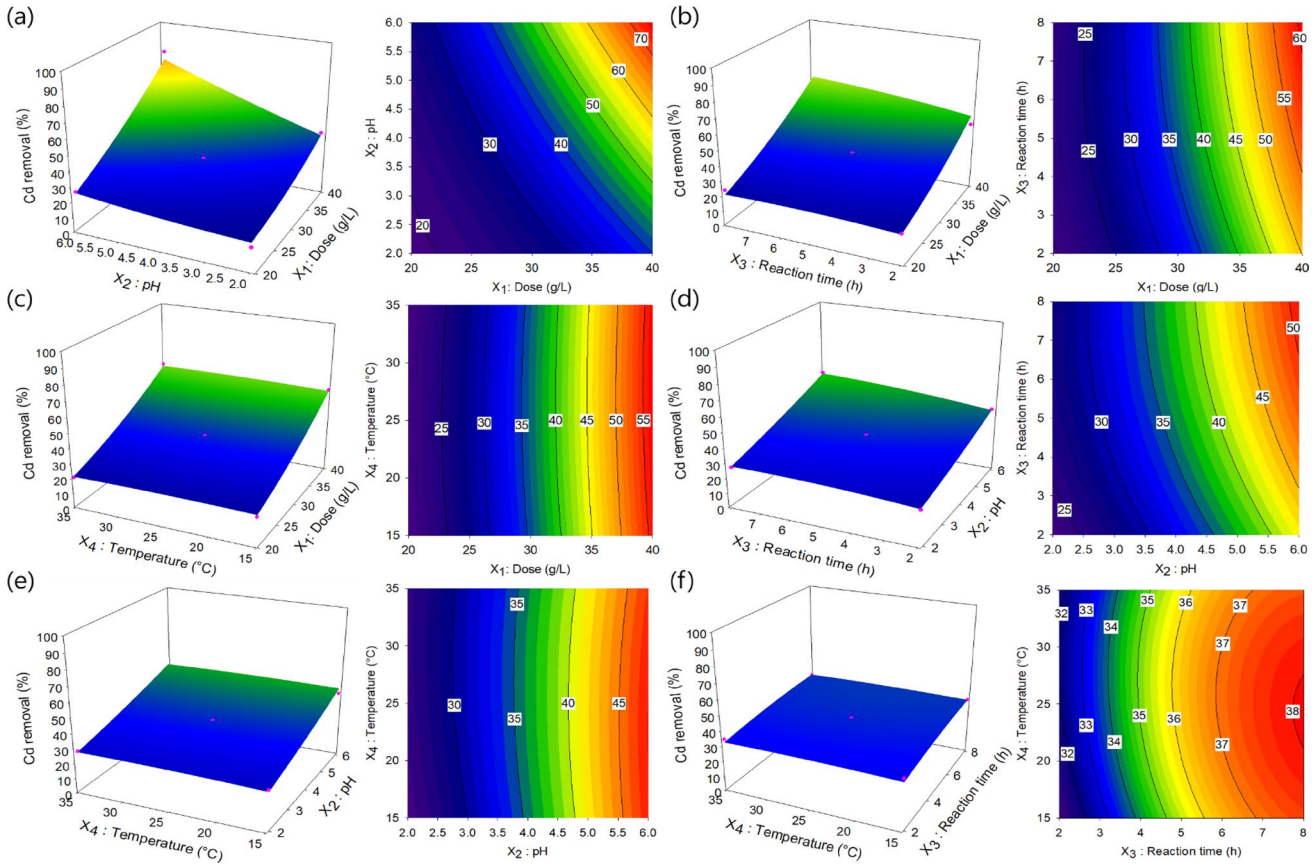

Fig. 6 Response surface methodology (RSM)-derived model illustrating Cd removal by PFSB–450. The figure presents three-dimensional response surface curves and corresponding contour plots for the following variable pairs: (a) Dose of PFSB–450 versus pH of industrial wastewater, (b) Dose of PFSB–450 versus reaction time, (c) Dose of PFSB–450 versus reaction temperature, (d) pH of industrial wastewater versus reaction time, (e) pH of industrial wastewater versus reaction temperature, and (f) reaction time versus reaction temperature

heavy metal adsorption, including Cd, because it influences the surface charge of the adsorbent, the extent of metal ionization, and competition with ions present in the solution (Kwikima et al. 2021). As such, pH optimization is essential for achieving effective Cd removal from industrial effluents (Pal and Pal 2017). At lower pH values, PFSB–450 surfaces exhibit increased positive charge, resulting in enhanced competition with Cd^{2+} ions and subsequently lower removal efficiencies (Kwikima et al. 2021). Conversely, higher pH levels render the adsorbent surface more negatively charged, thereby strengthening electrostatic attraction and increasing the adsorption of Cd^{2+} ions (Kayranli 2022).

Reaction time (X_3) has a positive impact on Cd removal efficiency, with extended contact periods between Cd ions and the PFSB–450 surface resulting in greater adsorption. Initially, rapid adsorption occurs because of the large number of available active sites and a steep concentration gradient (Othmani et al. 2022). Over an extended period, the continual occupation of adsorption sites leads to a decrease in adsorption rate and ultimately to equilibrium (Awual et al. 2018). The RSM analysis determined the optimal contact time for maximum Cd removal to be 7.94 h. This duration was longer than the 3 h contact time required to reach equilibrium, as determined from the kinetic experiments (Sect. "Kinetic and isotherm experiments on Cd adsorption by PFSB–450"). The increased adsorption duration needed for the RSM experiment is likely due to the use of authentic zinc smelter wastewater, where interfering ions and complex components may have postponed the attainment of adsorption equilibrium compared to the more controlled conditions in the kinetic study.

Conclusions

This study established a sustainable approach for cadmium remediation by converting *Perilla frutescens* stems, an agricultural residue typically discarded or burned in open fields, into a functional biochar adsorbent. Importantly, straightforward pyrolysis at 450 °C without subsequent chemical modification produced a biochar (PFSB–450) with high efficiency for Cd removal. Distinct from

previous research relying on synthetic solutions, this study validated the effectiveness of PFSB–450 using real zinc smelter wastewater, thereby enhancing the practical significance and applicability of the findings.

PFSB–450 displayed advantageous physicochemical characteristics, such as a high C/N ratio, low H/C ratio, substantial porosity, and a rich presence of oxygen-containing functional groups, all of which contributed significantly to its enhanced Cd adsorption capacity. The adsorption processes were accurately characterized by both Elovich and Langmuir models, indicating dominant chemisorption and monolayer adsorption mechanisms. Mechanistic investigation revealed that electrostatic attraction, ion exchange, and complexation with oxygen-bearing and aromatic groups (via Cd–O and Cd–π interactions) were central removal mechanisms. Additionally, response surface methodology demonstrated that adsorbent dose, pH level, and contact time had significant impacts on Cd removal, whereas temperature showed not influence. Under optimal conditions, PFSB–450 reached a maximum Cd removal efficiency of 80.84% in actual zinc smelter wastewater.

Compared to other biochar-based adsorbents documented in the literature, PFSB–450 delivered comparable or better adsorption performance for Cd without the need for chemical modifications or pretreatments, emphasizing its operational simplicity, cost-effectiveness, and suitability for environmental application. These results reveal the combined benefits of addressing both agricultural waste disposal and industrial wastewater treatment, thus providing substantial environmental advantages. Overall, this work proposes an innovative, affordable, and scalable strategy that aligns with circular economy principles, and positions PFSB–450 as a promising material for large-scale wastewater treatment with both ecological and economic merit.

Supplementary Information The online version contains supplementary material available at https://doi.org/10.1007/s13201-025-02673-1.

Funding This research was supported byaResearch Program (Project No. RS-2023-00229969) for Carbon Reduction Technology in Agricultural and Livestock Sectors funded by Rural Development Administration, Republic of Korea. This research was also supported by Agriculture and Food Convergence Technologies Program for Research Manpower Development (RS-2024-00400922).

Declarations

Author contributions Methods, data analysis, writing-original draft [Jae-In Lee]; Methods [Jun-SikJo];Softwareandinvestigation [Youn-JunLee];Writing-reviewing and editing [Chang-Gu Lee];Conceptualization, funding acquisition: [Young-Man Yoon]; Conceptualization, writing-reviewing and editing, supervision, funding acquisition [Seong-Jik Park]

Data availability All data generated or analyzed during this study are included in the published article.Datasets used and/or analyzed in the current study are available from the corresponding author upon reasonable request.

Conflicts of interest The authorshave no conflicts of interestto disclose

Declaration of generative AI in scientific writing During the preparation of this work,the authors used ChatGPT4.0 to improve readability and language of the manuscript.

References

Abdel-Rhman MH, El-Asmy AA, Ibrahim R, Hosny NM (2023) New Schiff base ligand and some of its coordination compounds: synthesis, spectral, molecular modeling and biological studies. J Mol Struct 1279:135023. https://doi.org/10.1016/j.molstruc.2023.135023

Ahmed A, Bakar MSA, Sukri RS, Hussain M, Farooq A, Moogi S, Park YK (2020) Sawdust pyrolysis from the furniture industry in an auger pyrolysis reactor system for biochar and bio-oil production. Energy Conv Manag 226:113502. https://doi.org/10.1016/j.enconman.2020.113502

Alrefaee SH, Aljohani M, Alkhamis K, Shaaban F, El-Desouky MG, El-Bindary AA, El-Bindary MA (2023) Adsorption and effective removal of organophosphorus pesticides from aqueous solution via novel metal-organic framework: Adsorption isotherms, kinetics, and optimization via Box-Behnken design. J Mol Liq 384:122206. https://doi.org/10.1016/j.molliq.2023.122206

Atta MM, Henaish AMA, Elbasiony AM, Taha EO, Dorgham AM (2022) Structural, optical, and thermal properties of PEO/PVP blend reinforced biochar. Opt Mater 127:112268. https://doi.org/10.1016/j.optmat.2022.112268

Awogbemi O, Von Kallon DV (2023) Progress in agricultural waste derived biochar as adsorbents for wastewater treatment. Appl Surf Sci Adv 18:100518. https://doi.org/10.1016/j.apsadv.2023.100518

Awual MR, Khraisheh M, Alharthi NH, Luqman M, Islam A, Karim MR, Rahman MM, Khaleque MA (2018) Efficient detection and adsorption of cadmium (II) ions using innovative nano-composite materials. Chem Eng J 343:118–127. https://doi.org/10.1016/j.cej.2018.02.116

Balmuk G, Videgain M, Manyà JJ, Duman G, Yanik J (2023) Effects of pyrolysis temperature and pressure on agronomic properties of biochar. J Anal Appl Pyrolysis 169:105858. https://doi.org/10.1016/j.jaap.2023.105858

Boulanouar L, Louhichi B, Hamdi W, Jellali S, L'taief B, Hamdi N, Rebouh NY, Houas A (2025) Parametric study of cadmium and nickel removal from synthetic and actual industrial wastewater industry by electrocoagulation using solar energy. J Water Process Eng 71:107261. https://doi.org/10.1016/j.jwpe.2025.107261

Chai JB, Au PI, Mubarak NM, Khalid M, Ng WPQ, Jagadish P, Walvekar R, Abdullah EC (2020) Adsorption of heavy metal from industrial wastewater onto low-cost Malaysian kaolin clay–based adsorbent. Environ Sci Pollut Res 27:13949–13962. https://doi.org/10.1007/s11356-020-07755-y

Chang H, Yang XY, Liang D, Chen ZQ, Liu X (2024) Enhanced removal of ammonium nitrogen from aqueous solutions using a novel biochar derived from millet shells through both static adsorption and dynamic column experiments. J Water Process Eng 58:104848. https://doi.org/10.1016/j.jwpe.2024.104848

Chen M, He F, Hu D, Bao C, Huang Q (2020) Broadened operating pH range for adsorption/reduction of aqueous Cr (VI) using biochar from directly treated jute (*Corchorus capsularis* L.) fibers by H_3PO_4. Chem Eng J 381:122739. https://doi.org/10.1016/j.cej.2019.122739

Chen F, Sun Y, Liang C, Yang T, Mi S, Dai Y, Yu M, Yao Q (2022) Adsorption characteristics and mechanisms of Cd^{2+} from aqueous solution by biochar derived from corn stover. Sci Rep 12:17714. https://doi.org/10.1038/s41598-022-22714-y

Cheng S, Liu Y, Xing B, Qin X, Zhang C, Xia H (2021) Lead and cadmium clean removal from wastewater by sustainable biochar derived from poplar saw dust. J Clean Prod 314:128074. https://doi.org/10.1016/j.jclepro.2021.128074

Cheng S, Zhao S, Guo H, Xing B, Liu Y, Zhang C, Ma M (2022) High-efficiency removal of lead/cadmium from wastewater by MgO modified biochar derived from crofton weed. Bioresour Technol 343:126081. https://doi.org/10.1016/j.biortech.2021.126081

Cho SH, Lee S, Kim Y, Song H, Lee J, Tsang YF, Chen WH, Park YK, Lee DJ, Jung S, Kwon EE (2023a) Applications of agricultural residue biochars to removal of toxic gases emitted from chemical plants: a review. Sci Total Environ 868:161655

Cho EJ, Kang JK, Lee CG, Bae S, Park SJ (2023b) Use of thermally activated Fenton sludge for Cd removal in zinc smelter wastewater: mechanism and feasibility of Cd removal. Environ Pollut 334:122166. https://doi.org/10.1016/j.envpol.2023.122166

Das SK, Ghosh GK, Avasthe RK, Sinha K (2021) Compositional heterogeneity of different biochar: effect of pyrolysis temperature and feedstocks. J Environ Manage 278:111501. https://doi.org/10.1016/j.jenvman.2020.111501

de Paula Protásio T, da Costa JS, Scatolino MV, Lima MDR, de Assis MR, da Silva MG, Bufalino L, Dias Junior AF, Trugilho PF (2022) Revealing the influence of chemical compounds on the pyrolysis of lignocellulosic wastes from the Amazonian production chains. Int J Environ Sci Technol 19:4491–4508. https://doi.org/10.1007/s13762-021-03416-w

Debnath S, Das R (2023) Strong adsorption of CV dye by Ni ferrite nanoparticles for waste water purification: fits well the pseudo second order kinetic and Freundlich isotherm model. Ceram Int 49:16199–16215. https://doi.org/10.1016/j.ceramint.2023.01.218

Fan M, Li C, Shao Y, Sun K, Zhang L, Zhang S, Ding K, Gholizadeh M, Hu X (2022) Impact of biochar catalyst on pyrolysis of biomass of the same origin. J Environ Chem Eng 10:108546. https://doi.org/10.1016/j.jece.2022.108546

Gan F, Cheng B, Jin Z, Dai Z, Wang B, Yang L, Jiang X (2021) Hierarchical porous biochar from plant-based biomass through selectively removing lignin carbon from biochar for enhanced removal of toluene. Chemosphere 279:130514. https://doi.org/10.1016/j.chemosphere.2021.130514

Gao Z, Shan D, He J, Huang T, Mao Y, Tan H, Shi H, Li T, Xie T (2023) Effects and mechanism on cadmium adsorption removal by $CaCl_2$-modified biochar from selenium-rich straw. Bioresour Technol 370:128563. https://doi.org/10.1016/j.biortech.2022.128563

Ge S, Zhao S, Wang L, Zhao Z, Wang S, Tian C (2024) Exploring adsorption capacity and mechanisms involved in cadmium removal from aqueous solutions by biochar derived from euhalophyte. Sci Rep 14:450. https://doi.org/10.1038/s41598-023-50525-2

Gu H, Lin W, Sun S, Wu C, Yang F, Ziwei Y, Chen N, Ren J, Zheng S (2021) Calcium oxide modification of activated sludge as a low-cost adsorbent: preparation and application in Cd (II) removal. Ecotoxicol Environ Saf 209:111760. https://doi.org/10.1016/j.ecoenv.2020.111760

Gupta AD, Rawat KP, Bhadauria V, Singh H (2021) Recent trends in the application of modified starch in the adsorption of heavy metals from water: a review. Carbohydr Polym 269:117763. https://doi.org/10.1016/j.carbpol.2021.117763

Igwilo CN, Ude NC, Onoh IM, Enekwe CB, Alieze BA (2022) RSM, ANN and ANFIS applications in modeling fermentable sugar production from enzymatic hydrolysis of *Colocynthis vulgaris* Shrad seeds shell. Bioresour Technol Rep 18:101056. https://doi.org/10.1016/j.biteb.2022.101056

Jeon J, Park JH, Wi S, Yang S, Ok YS, Kim S (2019) Characterization of biocomposite using coconut oil impregnated biochar as latent heat storage insulation. Chemosphere 236:124269. https://doi.org/10.1016/j.chemosphere.2019.06.239

Kang X, Sun M, Geng N, Li Y, Wang H, Pan H, Yang Q, Yang Z, Lou Y, Zhuge Y (2024) A novel and recyclable silica gel-modified biochar to remove cadmium from wastewater: model application and mechanism exploration. Ecotoxicol Environ Saf 281:116608. https://doi.org/10.1016/j.ecoenv.2024.116608

Kayranli B (2022) Cadmium removal mechanisms from aqueous solution by using recycled lignocelluloses. Alex Eng J 61:443–457. https://doi.org/10.1016/j.aej.2021.06.036

Khan ZH, Gao M, Qiu W, Islam MS, Song Z (2020) Mechanisms for cadmium adsorption by magnetic biochar composites in an aqueous solution. Chemosphere 246:125701. https://doi.org/10.1016/j.chemosphere.2019.125701

Khedulkar AP, Pandit B, Dang VD, Doong RA (2023) Agricultural waste to real worth biochar as a sustainable material for supercapacitor. Sci Total Environ 869:161441. https://doi.org/10.1016/j.scitotenv.2023.161441

Khelali A, Benmahdi F, Sahnoune D, Sami K, Hacıosmanoğlu GG, Akram S, Isinkaralar K, Siswanta D, Hosseini-Bandegharaei A (2025) Removal of AG 25 dye from aqueous solutions and treatment of real tannery wastewater by reusable magnetic iron oxide nanoparticles loaded with pomegranate pomace extract. Environ Res. https://doi.org/10.1016/j.envres.2025.121744

Khiari B, Ghouma I, Ferjani AI, Azzaz AA, Jellali S, Limousy L, Jeguirim M (2020) Kenaf stems: thermal characterization and conversion for biofuel and biochar production. Fuel 262:116654. https://doi.org/10.1016/j.fuel.2019.116654

Kolesnikov TI, Orlova AM, Drozdov FV, Buzin AI, Cherkaev GV, Kechekyan AS, Dmitryakov PV, Belousov SI, Kuznetsov AA (2022) New imide-based thermosets with propargyl ether groups for high temperature composite application. Polymer 254:125038. https://doi.org/10.1016/j.polymer.2022.125038

Kumar V, Dwivedi SK, Oh S (2022) A review on microbial-integrated techniques as promising cleaner option for removal of chromium, cadmium and lead from industrial wastewater. J Water Process Eng 47:102727. https://doi.org/10.1016/j.jwpe.2022.102727

Kwikima MM, Mateso S, Chebude Y (2021) Potentials of agricultural wastes as the ultimate alternative adsorbent for cadmium removal from wastewater. A review. Sci Afr 13:e00934. https://doi.org/10.1016/j.sciaf.2021.e00934

Lee YJ, Lee CG, Min KJ, Park SJ (2024a) Efficient cadmium removal from industrial wastewater generated from smelter using chemical precipitation and oxidation assistance. Water Environ Res 96:e11059. https://doi.org/10.1002/wer.11059

Lee JI, Choi D, Kim S, Kim JY, Park SJ, Kwon EE (2024b) Developing a sorptive material of cadmium from pyrolysis of hen manure. Chemosphere 351:141262. https://doi.org/10.1016/j.chemosphere.2024.141262

Lee JI, Jang SH, Kim C, Kang JK, Lee CG, Park SJ (2024c) Evaluation of large-scale poultry manure-derived biochar for efficient cadmium removal in zinc smelter wastewater. J Environ Manage 370:122763. https://doi.org/10.1016/j.jenvman.2024.122763

Lee YJ, Son CY, Jeong YJ, Cho IS, Park SJ, Lee CG (2024d) Cobalt (VI)-oxo species-mediated selective oxidation of electron-rich organic contaminants by Co-loaded hydroxylated g-C_3N_4 with high resistance to an inhibitory effect of background constituents. Appl Surf Sci 669:160545. https://doi.org/10.1016/j.apsusc.2024.160545

Leng L, Xiong Q, Yang L, Li H, Zhou Y, Zhang W, Jiang S, Li H, Huang H (2021) An overview on engineering the surface area and porosity of biochar. Sci Total Environ 763:144204. https://doi.org/10.1016/j.scitotenv.2020.144204

Li Y, Wang Z, Pan Z, Niu X, Yu Y, Meng S (2019) Pore structure and its fractal dimensions of transitional shale: a cross-section from east margin of the Ordos Basin, China. Fuel 241:417–431. https://doi.org/10.1016/j.fuel.2018.12.066

Li N, Rao F, He L, Yang S, Bao Y, Huang C, Bao M, Chen Y (2020) Evaluation of biochar properties exposing to solar radiation: a promotion on surface activities. Chem Eng J 384:123353. https://doi.org/10.1016/j.cej.2019.123353

Li J, Chen M, Yang X, Zhang L (2023) Preparation of a novel hydrogel of sodium alginate using rural waste bone meal for efficient adsorption of heavy metals cadmium ion. Sci Total Environ 863:160969. https://doi.org/10.1016/j.scitotenv.2022.160969

Li Z, Niu R, Yu J, Yu L, Cao D (2024) Removal of cadmium from aqueous solution by magnetic biochar: adsorption characteristics and mechanism. Environ Sci Pollut Res 31:6543–6557. https://doi.org/10.1007/s11356-023-31664-5

Liu B, Chen T, Wang B, Zhou S, Zhang Z, Li Y, Pan X, Wang N (2022a) Enhanced removal of Cd^{2+} from water by AHP-pretreated biochar: adsorption performance and mechanism. J Hazard Mater 438:129467. https://doi.org/10.1016/j.jhazmat.2022.129467

Liu Z, Zhen F, Zhang Q, Qian X, Li W, Sun Y, Zhang L, Qu B (2022b) Nanoporous biochar with high specific surface area based on rice straw digestion residue for efficient adsorption of mercury ion from water. Bioresour Technol 359:127471. https://doi.org/10.1016/j.biortech.2022.127471

Liu M, Liu X, Wu Z, Zhang Y, Meng Q, Yan L (2022c) Sulfur-modified *Pleurotus ostreatus* spent substrate biochar enhances the removal of cadmium in aqueous solution: characterization, performance, mechanism. J Environ Manage 322:115900. https://doi.org/10.1016/j.jenvman.2022.115900

Liu Y, Wang L, Liu C, Ma J, Ouyang X, Weng L, Chen Y, Li Y (2023) Enhanced cadmium removal by biochar and iron oxides composite: material interactions and pore structure. J Environ Manage 330:117136. https://doi.org/10.1016/j.jenvman.2022.117136

Lu Q, Wang Z, Wang J, Xie L, Liu Q, Zeng H (2023) Deciphering the specific interaction of humic acid with divalent cations at the nanoscale. Chem Eng J 470:144097. https://doi.org/10.1016/j.cej.2023.144097

Ma F, Zhao H, Zheng X, Zhao B, Diao J, Jiang Y (2023) Enhanced adsorption of cadmium from aqueous solution by amino modification biochar and its adsorption mechanism insight. J Environ Chem Eng 11:109747. https://doi.org/10.1016/j.jece.2023.109747

Mishra RK, Chinnam S, Sharma A (2025) Thermocatalytic pyrolysis of low-value waste biomass: thermal decomposition, kinetics behaviour, and biochar characterization. Results Eng 25:104210. https://doi.org/10.1016/j.rineng.2025.104210

Mohammad AT, Abdulhameed AS, Jawad AH (2019) Box-behnken design to optimize the synthesis of new crosslinked chitosan-glyoxal/TiO_2 nanocomposite: methyl orange adsorption and mechanism studies. Int J Biol Macromol 129:98–109. https://doi.org/10.1016/j.ijbiomac.2019.02.025

Narzari R, Poddar MK, Bordoloi N, Sarmah AK, Kataki R (2024) A comprehensive study to understand removal efficiency for Cr^{6+} using magnetic and activated biochar through response surface methodology. Biomass Convers Biorefin 14:5973–5987. https://doi.org/10.1007/s13399-021-01448-3

Nguyen DTC, Jalil AA, Hassan NS, Nguyen LM, Nguyen DH, Tran TV (2024) Optimization of hydrothermal synthesis conditions of Bidens pilosa–derived $NiFe_2O_4$@ AC for dye adsorption using response surface methodology and Box-Behnken design. Environ Sci Pollut Res. https://doi.org/10.1007/s11356-024-32691-6

Niazi NK, Bibi I, Shahid M, Ok YS, Burton ED, Wang H, Shaheen SM, Rinklebe J, Lüttge A (2018) Arsenic removal by perilla leaf biochar in aqueous solutions and groundwater: an integrated spectroscopic and microscopic examination. Environ Pollut 232:31–41. https://doi.org/10.1016/j.envpol.2017.09.051

Oginni O, Yakaboylu GA, Singh K, Sabolsky EM, Unal-Tosun G, Jaisi D, Khanal S, Shah A (2020) Phosphorus adsorption behaviors of MgO modified biochars derived from waste woody biomass resources. J Environ Chem Eng 8:103723. https://doi.org/10.1016/j.jece.2020.103723

Othmani A, Magdouli S, Kumar PS, Kapoor A, Chellam PV, Gökkuş Ö (2022) Agricultural waste materials for adsorptive removal of phenols, chromium (VI) and cadmium (II) from wastewater: a review. Environ Res 204:111916. https://doi.org/10.1016/j.envres.2021.111916

Pal P, Pal A (2017) Surfactant-modified chitosan beads for cadmium ion adsorption. Int J Biol Macromol 104:1548–1555. https://doi.org/10.1016/j.ijbiomac.2017.02.042

Panwar NL, Pawar A (2022) Influence of activation conditions on the physicochemical properties of activated biochar: a review. Biomass Convers Biorefin 12:925–947. https://doi.org/10.1007/s13399-020-00870-3

Pasumarthi R, Sawargaonkar G, Kale S, Kumar NV, Choudhari PL, Singh R, Davala MS, Rani CS, Mutnuri S, Jat ML (2024) Innovative bio-pyrolytic method for efficient biochar production from maize and pigeonpea stalks and their characterization. J Clean Prod 448:141573. https://doi.org/10.1016/j.jclepro.2024.141573

Polat S, Sayan P (2019) Application of response surface methodology with a Box-Behnken design for struvite precipitation. Adv Powder Technol 30:2396–2407. https://doi.org/10.1016/j.apt.2019.07.022

Rasapoor M, Young B, Asadov A, Brar R, Sarmah AK, Zhuang WQ, Baroutian S (2020) Effects of biochar and activated carbon on biogas generation: a thermogravimetric and chemical analysis approach. Energy Conv Manag 203:112221. https://doi.org/10.1016/j.enconman.2019.112221

Rechberger MV, Kloss S, Wang SL, Lehmann J, Rennhofer H, Ottner F, Wriessnig K, Daudin G, Lichtenegger H, Soja G, Zehetner F (2019) Enhanced Cu and Cd sorption after soil aging of woodchip-derived biochar: what were the driving factors? Chemosphere 216:463–471. https://doi.org/10.1016/j.chemosphere.2018.10.094

Sahu UK, Mahapatra SS, Patel RK (2018) Application of Box-Behnken design in response surface methodology for adsorptive removal of arsenic from aqueous solution using CeO_2/Fe_2O_3/graphene nanocomposite. Mater Chem Phys 207:233–242. https://doi.org/10.1016/j.matchemphys.2017.11.042

Segneanu AE, Marin CN, Vlase G, Cepan C, Mihailescu M, Muntean C, Grozescu I (2022) Highly efficient engineered waste

eggshell-fly ash for cadmium removal from aqueous solution. Sci Rep 12:9676. https://doi.org/10.1038/s41598-022-13664-6

Sekhon SS, Kaur P, Park JS (2021) From coconut shell biomass to oxygen reduction reaction catalyst: tuning porosity and nitrogen doping. Renew Sustain Energy Rev 147:111173. https://doi.org/10.1016/j.rser.2021.111173

Shewatatek S, Gonfa G, Mekuria S, Tessema B, Kezembayeva G, Ghosh KS, Mushtaq M, Diyanatizadeh MH, Isinkaralar K, Hosseini-Bandegharaei A (2025) Synthesis of diatomite/Fe_3O_4/Teff straw activated carbon composite adsorbent for Cr(VI) removal from wastewater. Results Chem. https://doi.org/10.1016/j.rechem.2025.102486

Tan WT, Zhou H, Tang SF, Zeng P, Gu JF, Liao BH (2022) Enhancing Cd(II) adsorption on rice straw biochar by modification of iron and manganese oxides. Environ Pollut 300:118899. https://doi.org/10.1016/j.envpol.2022.118899

Teng D, Zhang B, Xu G, Wang B, Mao K, Wang J, Sun J, Feng X, Yang Z, Zhang H (2020) Efficient removal of Cd(II) from aqueous solution by pinecone biochar: sorption performance and governing mechanisms. Environ Pollut 265:115001. https://doi.org/10.1016/j.envpol.2020.115001

Thangaraj B, Wongyao N, Solomon PR, Gupta V, Abdullah A, Abedrabbo S, Hassan J (2024) Synthesis of reduced graphene oxide from onion peel waste by single-stage pyrolysis, characterization and evaluation of its antibacterial activity. J Environ Chem Eng 12:113474. https://doi.org/10.1016/j.jece.2024.113474

Tomczyk A, Sokołowska Z, Boguta P (2020) Biomass type effect on biochar surface characteristic and adsorption capacity relative to silver and copper. Fuel 278:118168. https://doi.org/10.1016/j.fuel.2020.118168

Vareda JP (2023) On validity, physical meaning, mechanism insights and regression of adsorption kinetic models. J Mol Liq 376:121416. https://doi.org/10.1016/j.molliq.2023.121416

Vikraman VK, Kumar DP, Boopathi G, Subramanian P (2021) Kinetic and thermodynamic study of finger millet straw pyrolysis through thermogravimetric analysis. Bioresour Technol 342:125992. https://doi.org/10.1016/j.biortech.2021.125992

Wang J, Guo X (2020) Adsorption kinetic models: Physical meanings, applications, and solving methods. J Hazard Mater 390:122156. https://doi.org/10.1016/j.jhazmat.2020.122156

Wang X, Dang Z, Hou S, Yuan Y, Wang X, Pan S (2022a) Fractal characteristics of pulverized high volatile bituminous coals with different particle size using gas adsorption. Fuel 315:122814. https://doi.org/10.1016/j.fuel.2021.122814

Wang L, Olsen MNP, Moni C, Dieguez-Alonso A, de la Rosa JM, Stenrød M, Liu X, Mao L (2022b) Comparison of properties of biochar produced from different types of lignocellulosic biomass by slow pyrolysis at 600 °C. Appl Energy Combust Sci 12:100090. https://doi.org/10.1016/j.jaecs.2022.100090

Waqas M, Aburiazaiza AS, Miandad R, Rehan M, Barakat MA, Nizami AS (2018) Development of biochar as fuel and catalyst in energy recovery technologies. J Clean Prod 188:477–488. https://doi.org/10.1016/j.jclepro.2018.04.017

Wu J, Wang T, Zhang Y, Pan WP (2019) The distribution of Pb (II)/Cd (II) adsorption mechanisms on biochars from aqueous solution: considering the increased oxygen functional groups by HCl treatment. Bioresour Technol 291:121859. https://doi.org/10.1016/j.biortech.2019.121859

Wu P, Cui P, Zhang Y, Alves ME, Liu C, Zhou D, Wang Y (2022) Unraveling the molecular mechanisms of Cd sorption onto MnOx-loaded biochar produced from the Mn-hyperaccumulator *Phytolacca americana*. J Hazard Mater 423:127157. https://doi.org/10.1016/j.jhazmat.2021.127157

Xu S, Chen J, Peng H, Leng S, Li H, Qu W, Hu Y, Li H, Jiang S, Zhou W, Leng L (2021) Effect of biomass type and pyrolysis temperature on nitrogen in biochar, and the comparison with hydrochar. Fuel 291:120128. https://doi.org/10.1016/j.fuel.2021.120128

Xu Y, Xia H, Zhang Q, Jiang G, Cai W, Hu W (2022) Adsorption of cadmium (II) in wastewater by magnesium oxide modified biochar. Arab J Chem 15:104059. https://doi.org/10.1016/j.arabjc.2022.104059

Yuan S, Hong M, Li H, Ye Z, Gong H, Zhang J, Huang Q, Tan Z (2020) Contributions and mechanisms of components in modified biochar to adsorb cadmium in aqueous solution. Sci Total Environ 733:139320. https://doi.org/10.1016/j.scitotenv.2020.139320

Yuan J, Zhu Y, Wang J, Liu Z, He M, Zhang T, Li P, Qiu F (2021) Facile modification of biochar derived from agricultural straw waste with effective adsorption and removal of phosphorus from domestic sewage. J Inorg Organomet Polym Mater 31:3867–3879. https://doi.org/10.1007/s10904-021-01992-5

Zhang D, Zhang K, Hu X, He Q, Yan J, Xue Y (2021) Cadmium removal by $MgCl_2$ modified biochar derived from crayfish shell waste: batch adsorption, response surface analysis and fixed bed filtration. J Hazard Mater 408:124860. https://doi.org/10.1016/j.jhazmat.2020.124860

Zhou Z, Huang L, Wang H, Chen Y (2024) Efficient removal of cadmium and lead in water by using nano-manganese oxide-loaded hydrochloric acid pretreated biochar. J Environ Chem Eng 12:113548. https://doi.org/10.1016/j.jece.2024.113548

Zhou Q, Huang Y, Liu L, Li Z, Xiao Y, Li Z, Tian T, Pan H (2025) Enhanced cadmium adsorption by silicate-modified biochar derived from sawdust: mechanisms and performance analysis. Surf Interfaces 65:106430. https://doi.org/10.1016/j.surfin.2025.106430